## Appendix for:

# A spontaneous termination mechanism of RNA polymerase V shapes the DNA methylation landscape in plants

**Table of Contents**

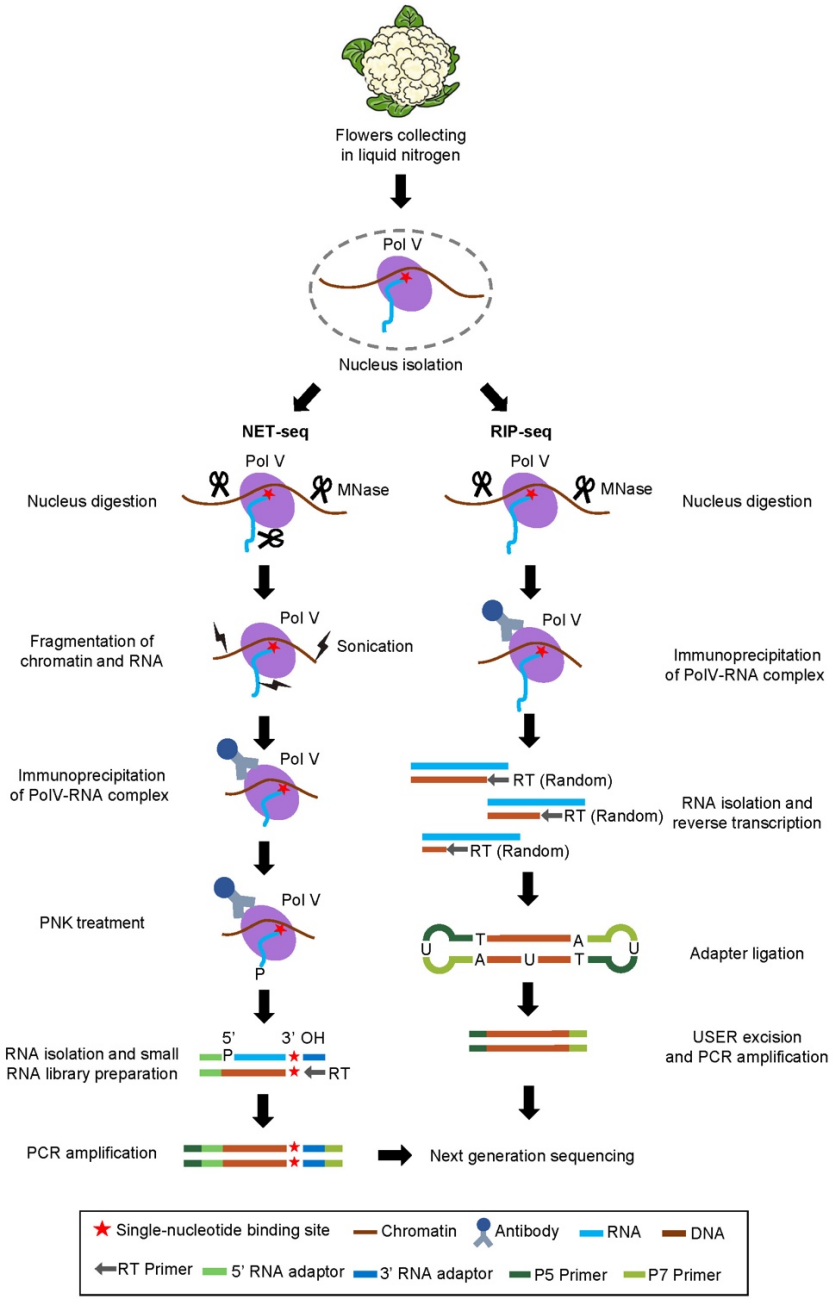


**Appendix Figure S1. A diagram of the experimental procedure of Pol V NET-seq and RIP-seq.**

In brief, nuclei were isolated from flower tissue and used for NET-seq and RIP-seq. For NET-seq, the RNA was fragmented by MNase treatment and sonication before being subjected to immunoprecipitation using a Pol V antibody. The RNA was adapter-ligated at both ends, reverse-transcribed, and amplified to generate the sequencing library following a small RNA-seq library generation protocol. For RIP-seq, the immunoprecipitation was performed without prior RNA fragmentation by sonication, and RNase inhibitor was added to keep the integrity of the long RNAs. The immunoprecipitated RNA was reverse-transcribed using random primers. The strand-specific sequencing library was then constructed using the dUTP method.

A

| | Samples | Raw reads | Clean reads | Mapped reads | Uniquely mapped reads | Remove duplication | Remove rRNA | Remove ChrCM | Remove tRNA | Mean insert length (bp) |
|---|---|---|---|---|---|---|---|---|---|---|
| Pol V-NET-seq | Rep1 | 127,470,964 | 125,001,582 | 111,376,109 | 21,908,291 | 3,735,621 | 3,689,179 | 3,642,054 | 3,640,420 | 31 |
| | Rep2 | 135,203,067 | 133,040,593 | 121,387,975 | 24,300,053 | 4,003,850 | 3,955,511 | 3,903,061 | 3,901,465 | 31 |
| Pol V-RIP-seq | Rep1 | 27,816,600 | 27,633,250 | 15,420,958 | 7,369,568 | - | 7,195,659 | 7,163,394 | 7,163,376 | 240 |
| | Rep2 | 35,269,266 | 35,038,541 | 19,731,972 | 9,139,382 | - | 8,922,588 | 8,882,543 | 8,882,527 | 204 |
| | Rep3 | 24,966,900 | 24,804,630 | 14,086,837 | 6,389,468 | - | 6,246,238 | 6,218,974 | 6,218,932 | 204 |

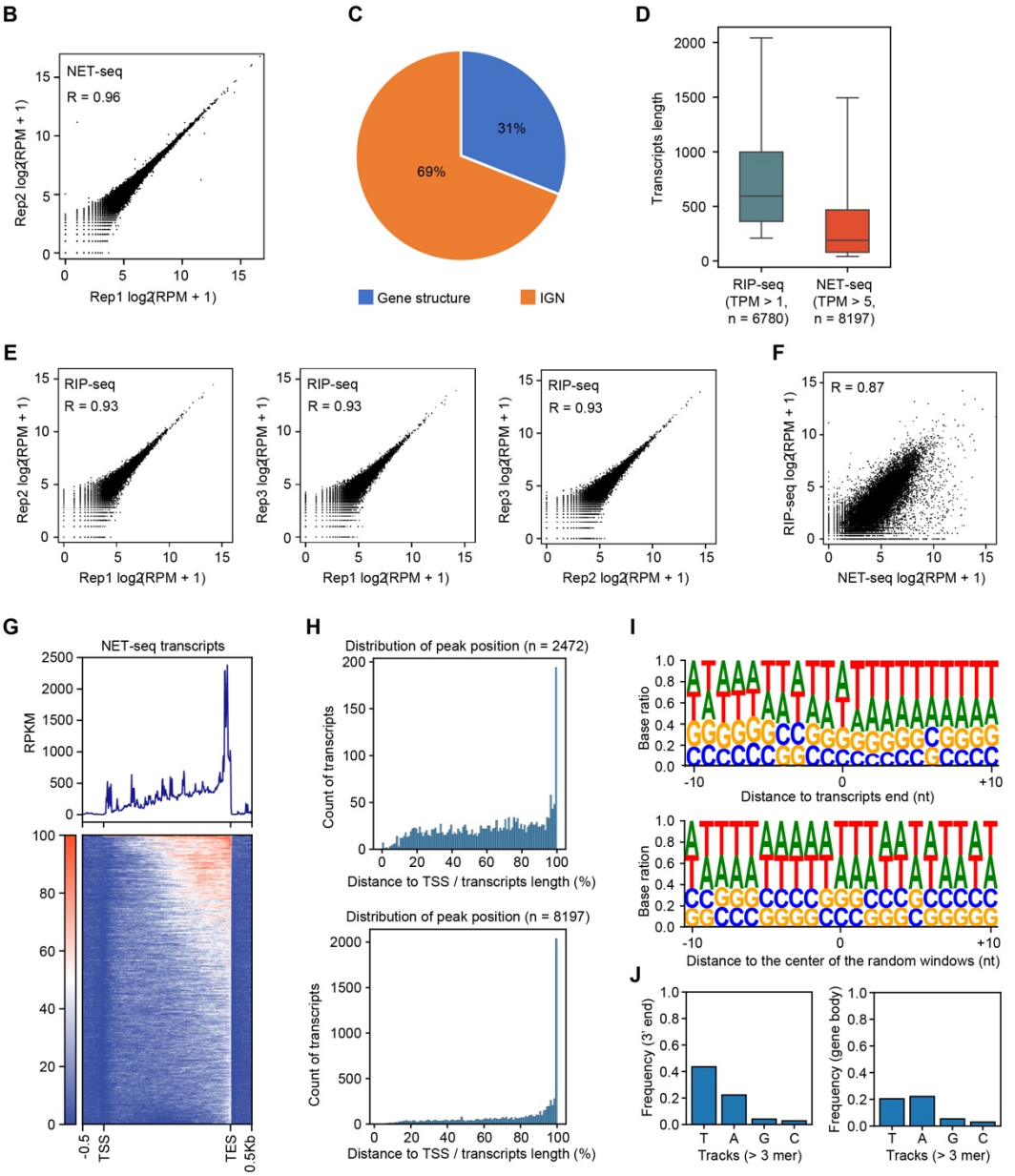


**Appendix Figure S2. Statistics of the Pol V NET-seq and RIP-seq data.**
**(A)** Summary of cauliflower Pol V NET-seq and RIP-seq data generated in this study. **(B)** Reproducibility of NET-seq data across the whole genome as calculated by using non-overlapped 10-kb windows for two independent biological replicates. Spearman correlation coefficients are indicated. **(C)** Pie chart showing the ratio of NET-seq reads mapped to gene structure and intergenic region (IGN). **(D)** The distribution of

transcripts length of RIP-seq and NET-seq. Boxplots show the median, with the bottom and top edges of the box representing the 25th and 75th percentiles, respectively. **(E)** Reproducibility of RIP-seq data across the whole genome as calculated by using non-overlapped 10-kb windows for three independent biological replicates. Spearman correlation coefficients are indicated. **(F)** Scatter plot demonstrates the correlation between RIP-seq and NET-seq data across the whole genome as calculated by using non-overlapped 10-kb windows. Replicates are merged to calculate RPM (reads per million). Spearman correlation coefficients are indicated. **(G)** Metagene plot showing the Pol V positioning along all 8,197 NET-seq data assembled transcripts. **(H)** The distribution of the positions with the highest Pol V NET-seq signal along each transcript. Results for 2472 transcripts and all 8197 transcripts were shown in the top and the bottom panels, respectively. **(I)** Sequence logos at the top showing the nucleotide ratio of the 21-nt region around the NET-seq transcript end sites. The x-axis refers to the distance to transcripts end sites; -10 and +10 mean the positions of 10-nt upstream or downstream of transcripts end sites, respectively. The heights of letters reflect the nucleotide ratio at each position calculated from the top 1000 NET-seq transcripts with the highest TPM (transcripts per million). The sequence logos at the bottom showing the nucleotide ratio of randomly selected 21-nt windows within the NET-seq transcript bodies. **(J)** Frequencies of motifs containing at least four consecutive T/A/C/G residues at Pol V transcript 3′ ends (±20 nt, non-template strand, top panel) or within transcript bodies (bottom panel).

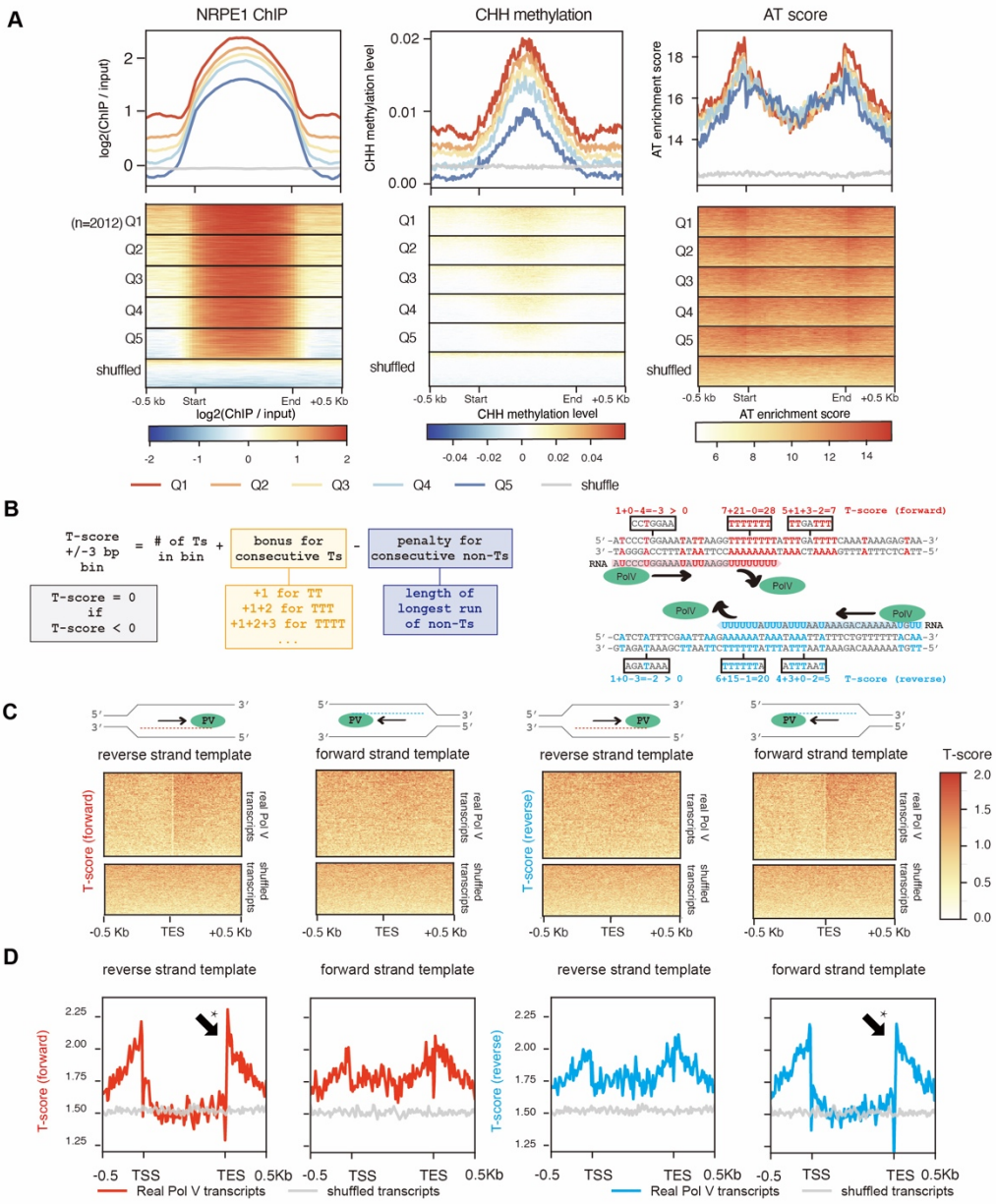


**Appendix Figure S3. Arabidopsis Pol V transciption boundaries enrich T-rich sequence.**

**(A)** Metaplot and heatmap representing NRPE1 ChIP-seq signal, AT enrichment signal and CHH methylation signal over NRPE1 ChIP peaks (n=10063) and shuffled regions. The NRPE1 ChIP peaks were evenly divided to five quantiles based on the rank of the NRPE1 ChIP-seq signal. **(B)** Diagram showing the way T-score was calculated on forward and reverse strands. **(C)** Heatmaps over Arabidopsis Pol V transcript end sites (TES) of T-score of either forward (left) or reverse (right) strand. Pol V transcripts transcribed using the forward and reverse strands as template were plotted separately. **(D)** Metaplots over Arabidopsis Pol V transcript from published RIP-seq data, of T-score of either forward (left) or reverse (right) strand. Note that all metaplots are oriented relative to transcription direction, so that the left part of metaplot corresponds to sequences before termination, and the right part after termination. Pol V transcripts

transcribed using the forward and reverse strands as template were plotted separately. *p-value < 2.2e-16, Welch Two-Sample t-test (50 bp regions upstream TES compared to 50 bp regions downstream TES).

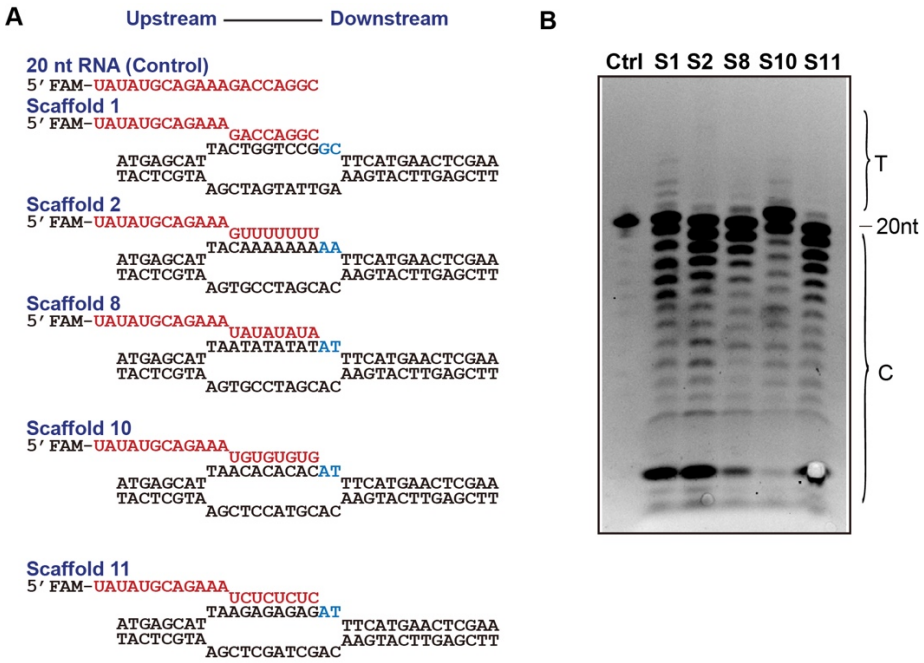


**Appendix Figure S4. *In vitro* Pol V transcription assay with designed scaffolds.** **(A)** The sequence of the designed scaffold for the *in vitro* assays. **(B)** Transcription assay shows that GA, TA, or CA repeat-containing $DNA_T$ can arrest Pol V elongation or fail to initiate transcription elongation, in a similar way as poly(A)-containing $DNA_T$. All *in vitro* assays were performed with at least 3 biological repeats, with similar results.

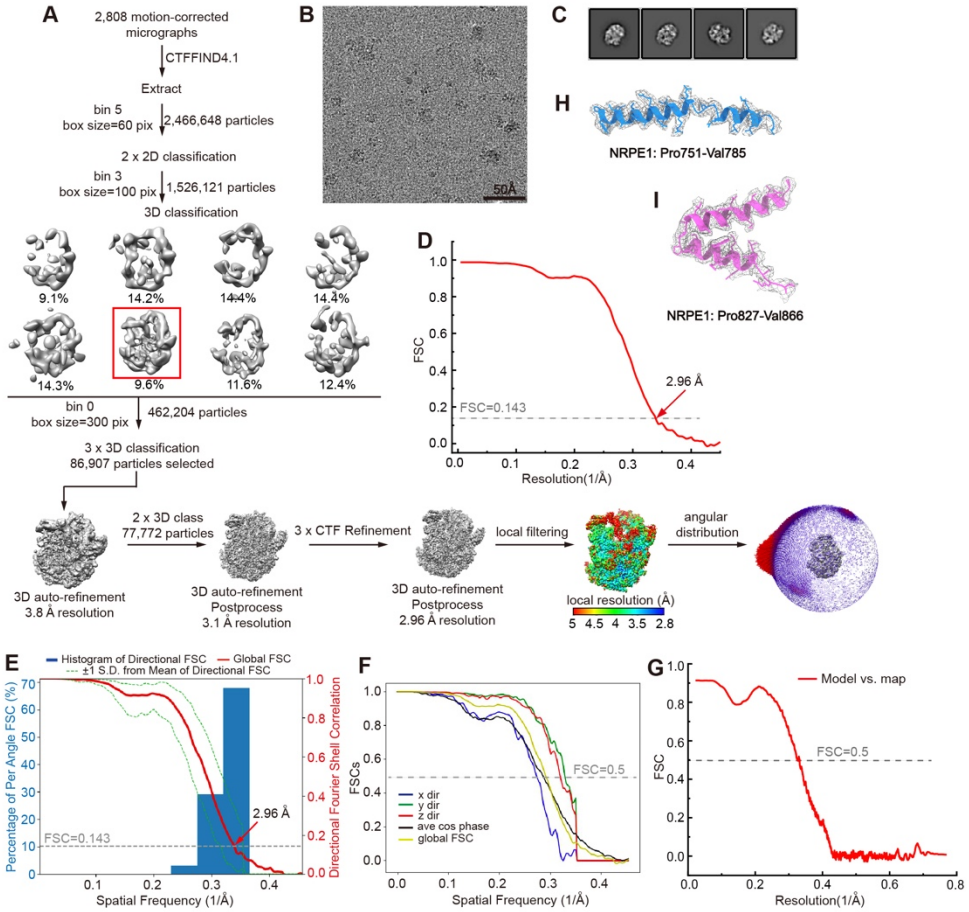


**Appendix Figure S5. Cryo-EM structure analysis of the 0U complex.**

**(A)** The flowchart for the data processing, including the local resolution map and angular distribution of particles of the final 3D reconstruction. **(B)** A representative image of the cryo-EM micrograph. **(C)** 2D class averages. **(D)** The FSC curves of the final 3D reconstruction. **(E-F)** The global (E) and directional (F) FSC of the 3D auto-refinement by the 3DFSC Processing Server. **(G)** The FSC calculated between the refined structure and the full map used for refinement. **(H-I)** Electron density maps showed the fitting of representative regions. The map is shown at the same contour level as in Fig. 4C.

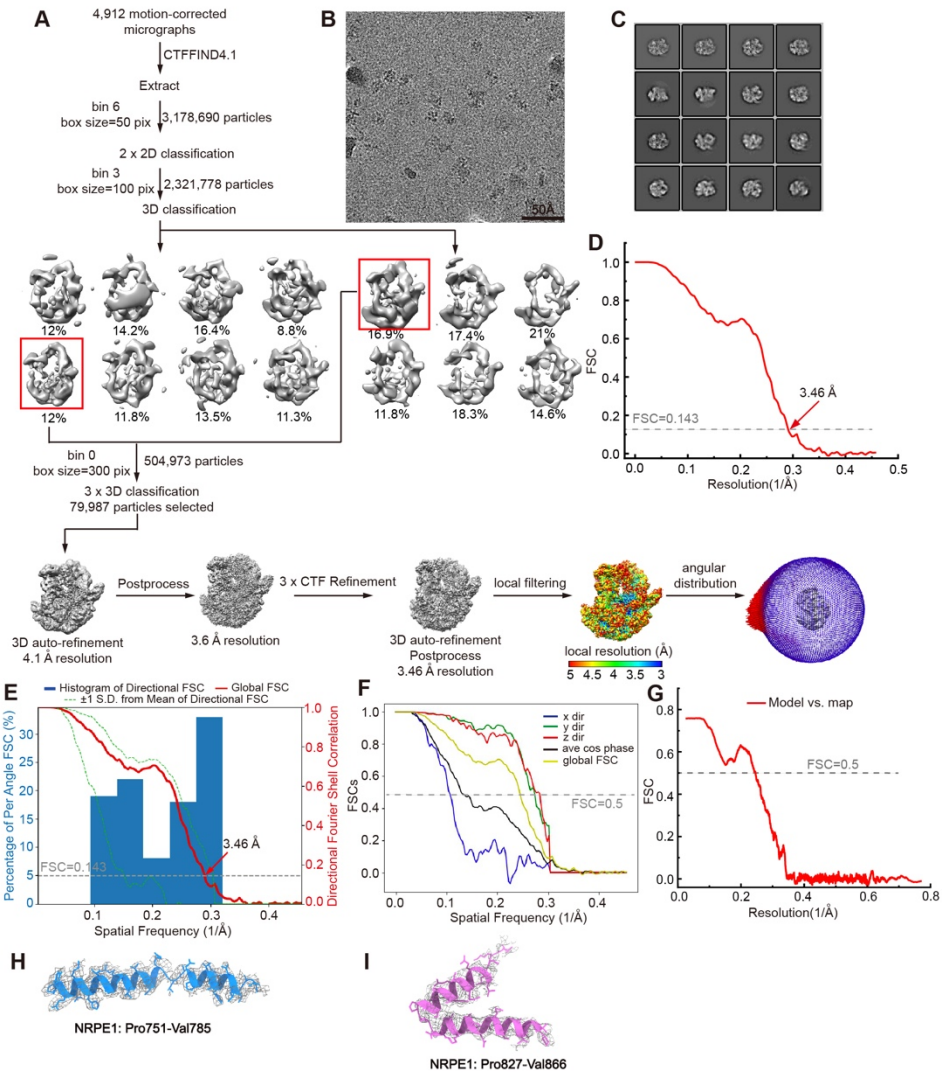


**Appendix Figure S6. Cryo-EM structure analysis of the 1U complex.**

**(A)** The flowchart for the data processing, including the local resolution map and angular distribution of particles of the final 3D reconstruction. **(B)** A representative image of the cryo-EM micrograph. **(C)** 2D class averages. **(D)** The FSC curves of the final 3D reconstruction. **(E-F)** The global (E) and directional (F) FSC of the 3D auto-refinement by the 3DFSC Processing Server. **(G)** The FSC calculated between the refined structure and the full map used for refinement. **(H-I)** Electron density maps showed the fitting of representative regions. The map is shown at the same contour level as in Fig. 4D.

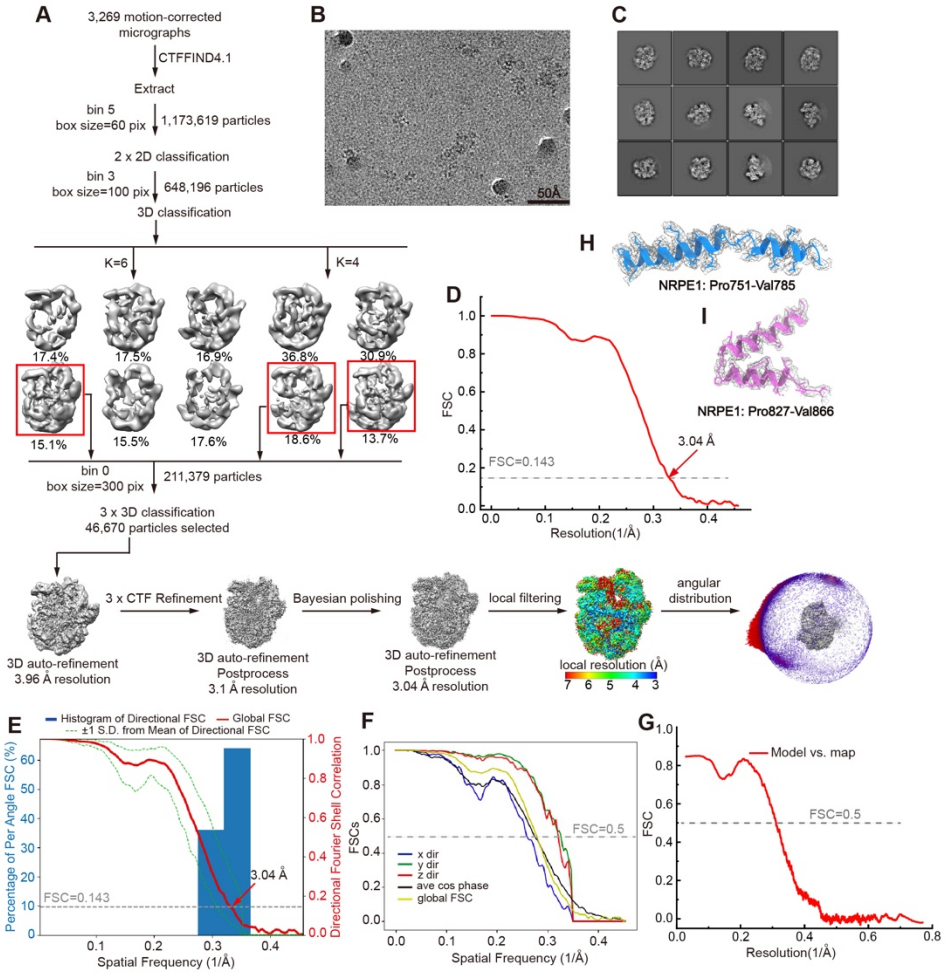


**Appendix Figure S7. Cryo-EM structure analysis of the 2U complex.**

**(A)** The flowchart for the data processing, including the local resolution map and angular distribution of particles of the final 3D reconstruction. **(B)** A representative image of the cryo-EM micrograph. **(C)** 2D class averages. **(D)** The FSC curves of the final 3D reconstruction. **(E-F)** The global (E) and directional (F) FSC of the 3D auto-refinement by the 3DFSC Processing Server. **(G)** The FSC calculated between the refined structure and the full map used for refinement. **(H-I)** Electron density maps showed the fitting of representative regions. The map is shown at the same contour level as in Fig. 4E.

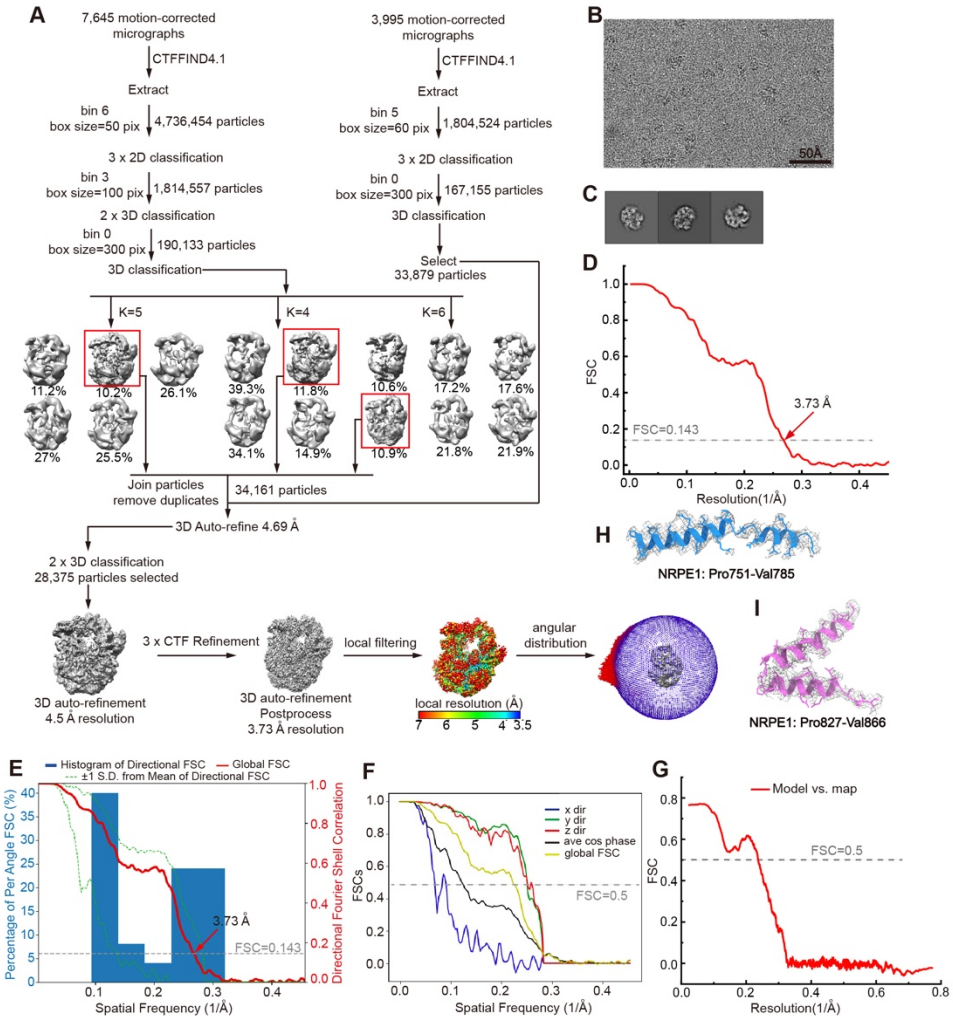


**Appendix Figure S8. Cryo-EM structure analysis of the 3U complex.**

**(A)** The flowchart for the data processing, including the local resolution map and angular distribution of particles of the final 3D reconstruction. **(B)** A representative image of the cryo-EM micrograph. **(C)** 2D class averages. **(D)** The FSC curves of the final 3D reconstruction. **(E-F)** The global (E) and directional (F) FSC of the 3D auto-refinement by the 3DFSC Processing Server. **(G)** The FSC calculated between the refined structure and the full map used for refinement. **(H-I)** Electron density maps showed the fitting of representative regions. The map is shown at the same contour level as in Fig. 4F.

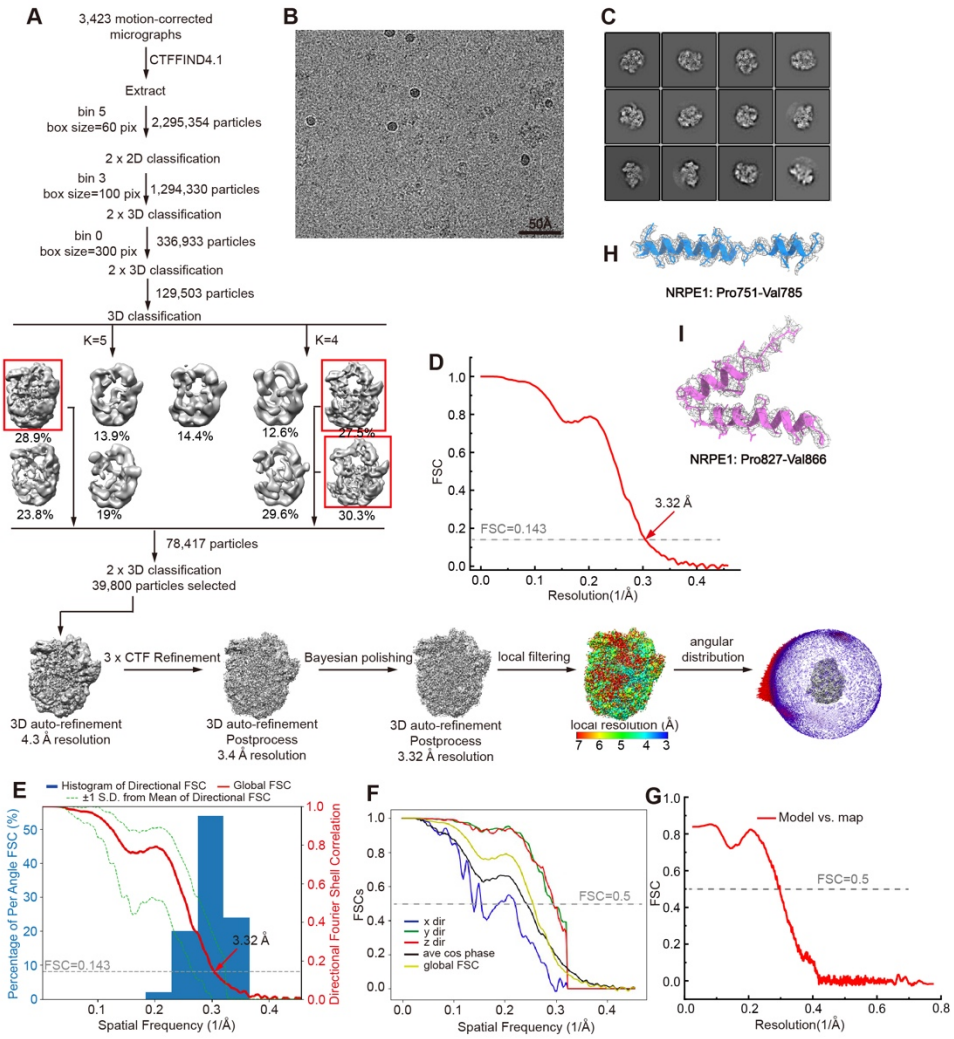


**Appendix Figure S9. Cryo-EM structure analysis of the 4U complex.**

**(A)** The flowchart for the data processing, including the local resolution map and angular distribution of particles of the final 3D reconstruction. **(B)** A representative image of the cryo-EM micrograph. **(C)** 2D class averages. **(D)** The FSC curves of the final 3D reconstruction. **(E-F)** The global (E) and directional (F) FSC of the 3D auto-refinement by the 3DFSC Processing Server. **(G)** The FSC calculated between the refined structure and the full map used for refinement. **(H-I)** Electron density maps showed the fitting of representative regions. The map is shown at the same contour level as in Fig. 4G.

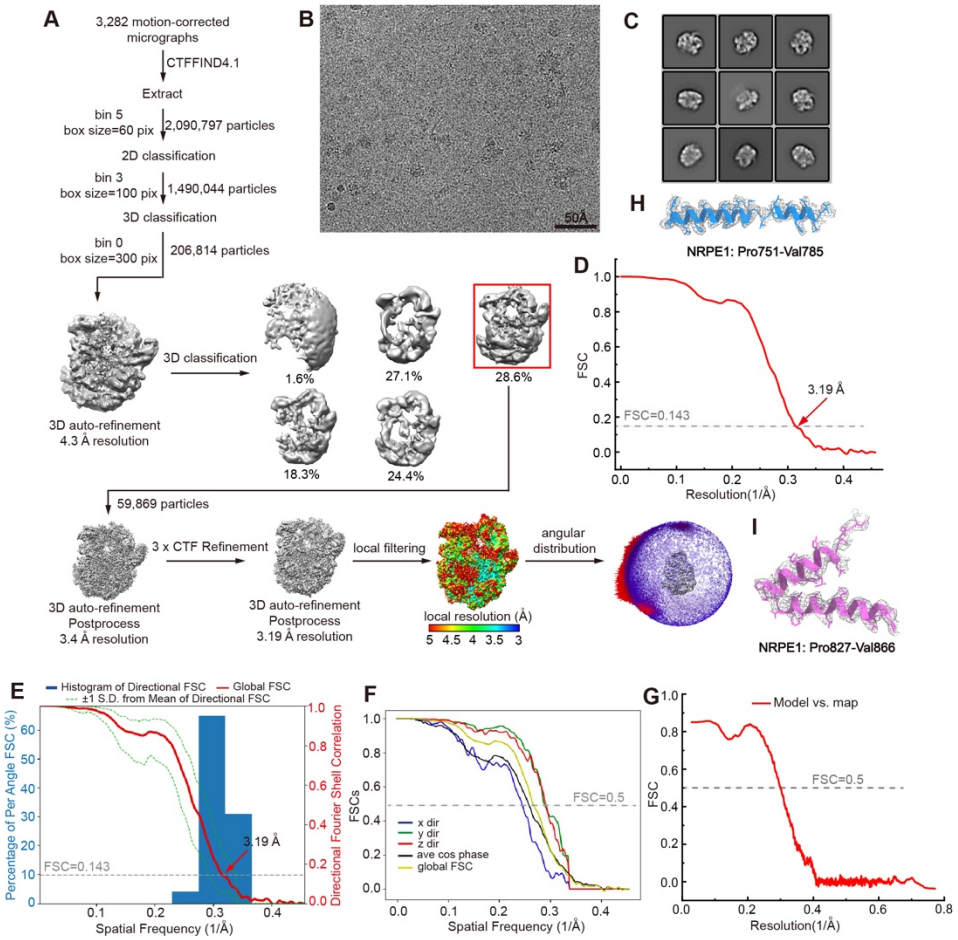


**Appendix Figure S10. Cryo-EM structure analysis of the 5U complex.**

**(A)** The flowchart for the data processing, including the local resolution map and angular distribution of particles of the final 3D reconstruction. **(B)** A representative image of the cryo-EM micrograph. **(C)** 2D class averages. **(D)** The FSC curves of the final 3D reconstruction. **(E-F)** The global (E) and directional (F) FSC of the 3D auto-refinement by the 3DFSC Processing Server. **(G)** The FSC calculated between the refined structure and the full map used for refinement. **(H-I)** Electron density maps showed the fitting of representative regions. The map is shown at the same contour level as in Fig. 4H.

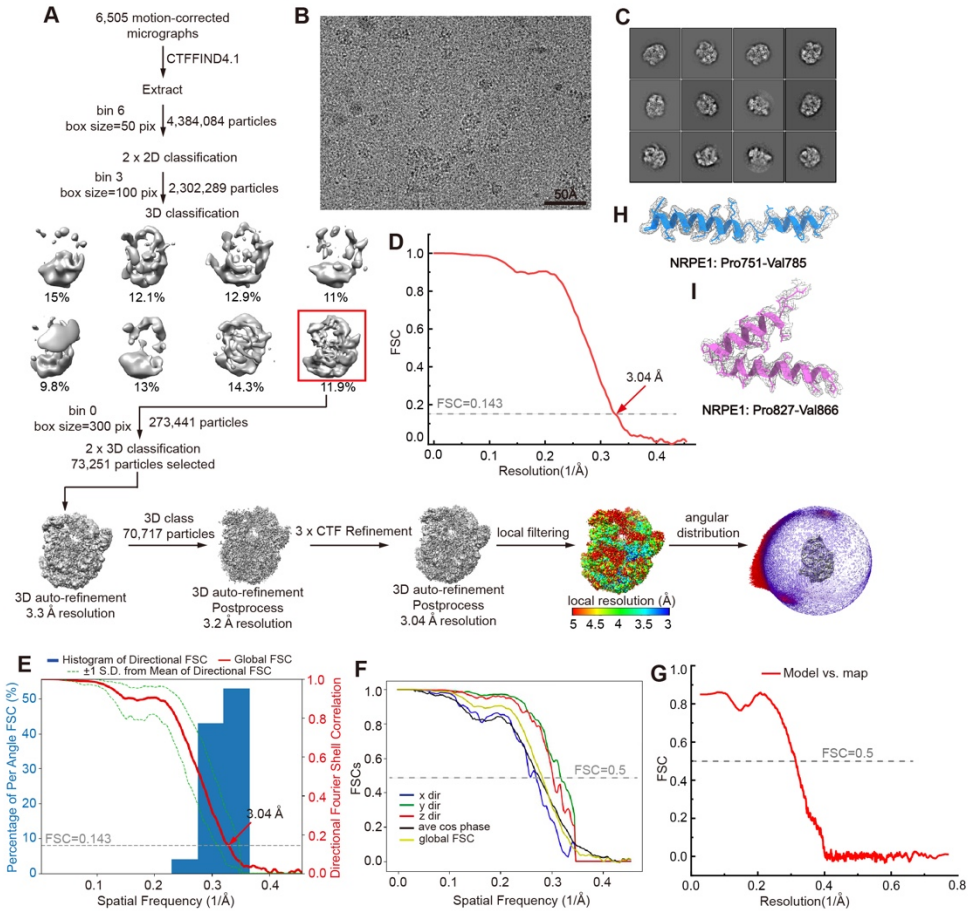


**Appendix Figure S11. Cryo-EM structure analysis of the 6U complex.**

**(A)** The flowchart for the data processing, including the local resolution map and angular distribution of particles of the final 3D reconstruction. **(B)** A representative image of the cryo-EM micrograph. **(C)** 2D class averages. **(D)** The FSC curves of the final 3D reconstruction. **(E-F)** The global (E) and directional (F) FSC of the 3D auto-refinement by the 3DFSC Processing Server. **(G)** The FSC calculated between the refined structure and the full map used for refinement. **(H-I)** Electron density maps showed the fitting of representative regions. The map is shown at the same contour level as in Fig. 4I.

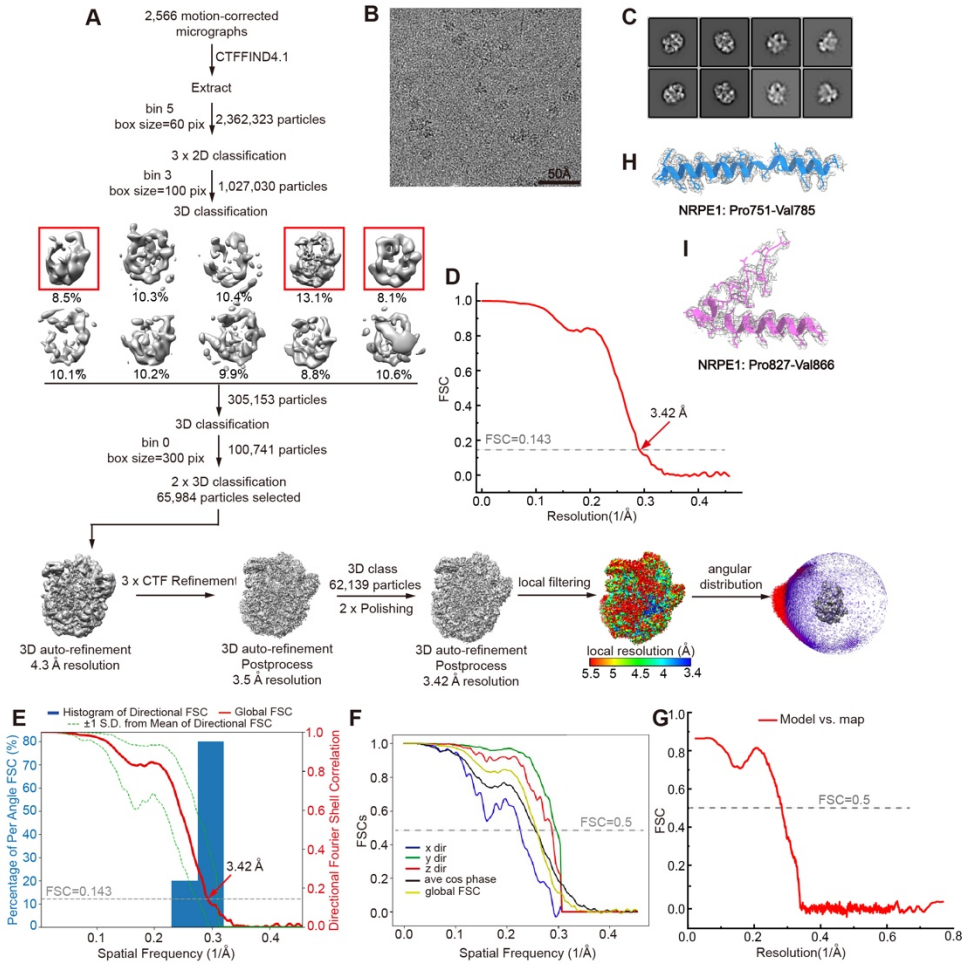


**Appendix Figure S12. Cryo-EM structure analysis of the 7U complex.**

**(A)** The flowchart for the data processing, including the local resolution map and angular distribution of particles of the final 3D reconstruction. **(B)** A representative image of the cryo-EM micrograph. **(C)** 2D class averages. **(D)** The FSC curves of the final 3D reconstruction. **(E-F)** The global (E) and directional (F) FSC of the 3D auto-refinement by the 3DFSC Processing Server. **(G)** The FSC calculated between the refined structure and the full map used for refinement. **(H-I)** Electron density maps showed the fitting of representative regions. The map is shown at the same contour level as in Fig. 4J.

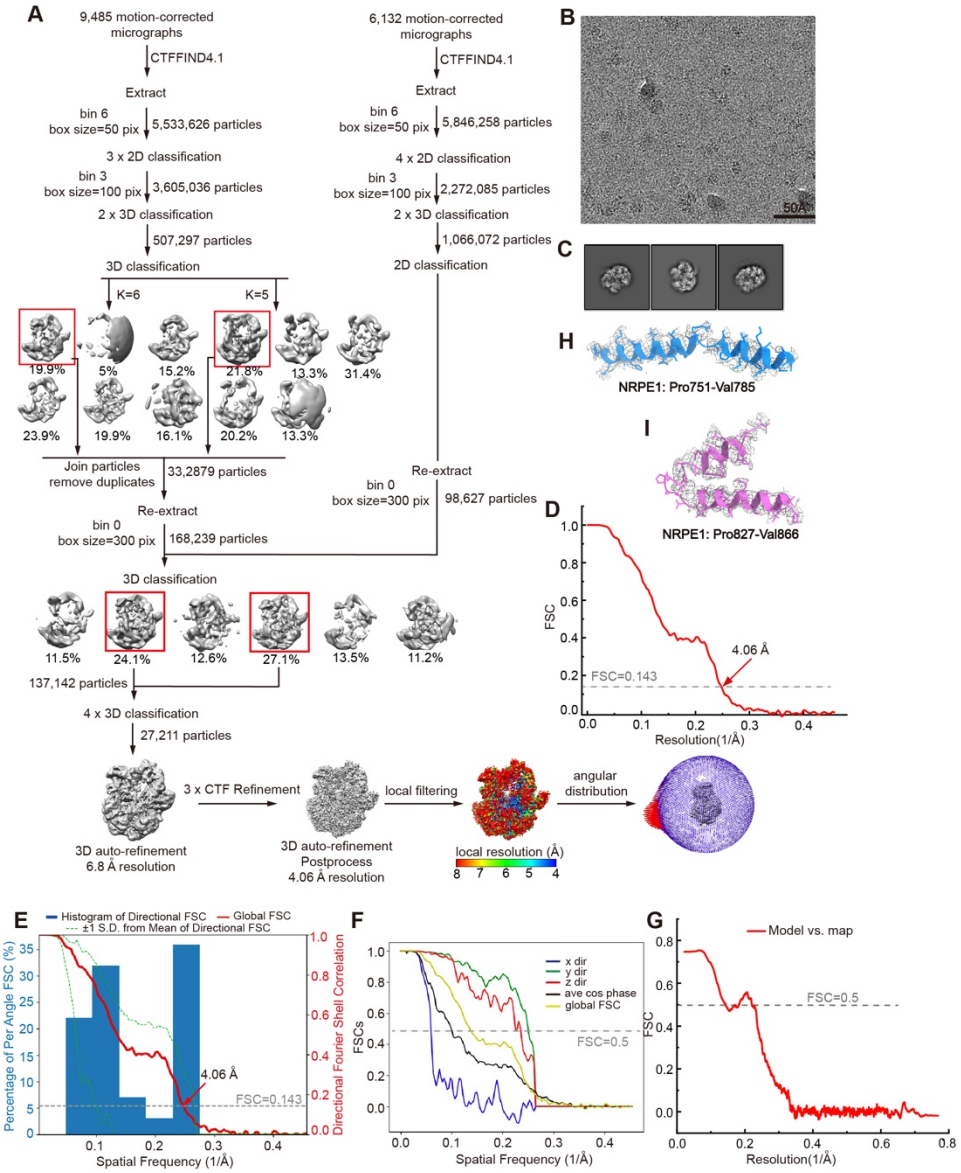


**Appendix Figure S13. Cryo-EM structure analysis of the 8U complex.**

**(A)** The flowchart for the data processing, including the local resolution map and angular distribution of particles of the final 3D reconstruction. **(B)** A representative image of the cryo-EM micrograph. **(C)** 2D class averages. **(D)** The FSC curves of the final 3D reconstruction. **(E-F)** The global (E) and directional (F) FSC of the 3D auto-refinement by the 3DFSC Processing Server. **(G)** The FSC calculated between the refined structure and the full map used for refinement. **(H-I)** Electron density maps showed the fitting of representative regions. The map is shown at the same contour level as in Fig. 4K.

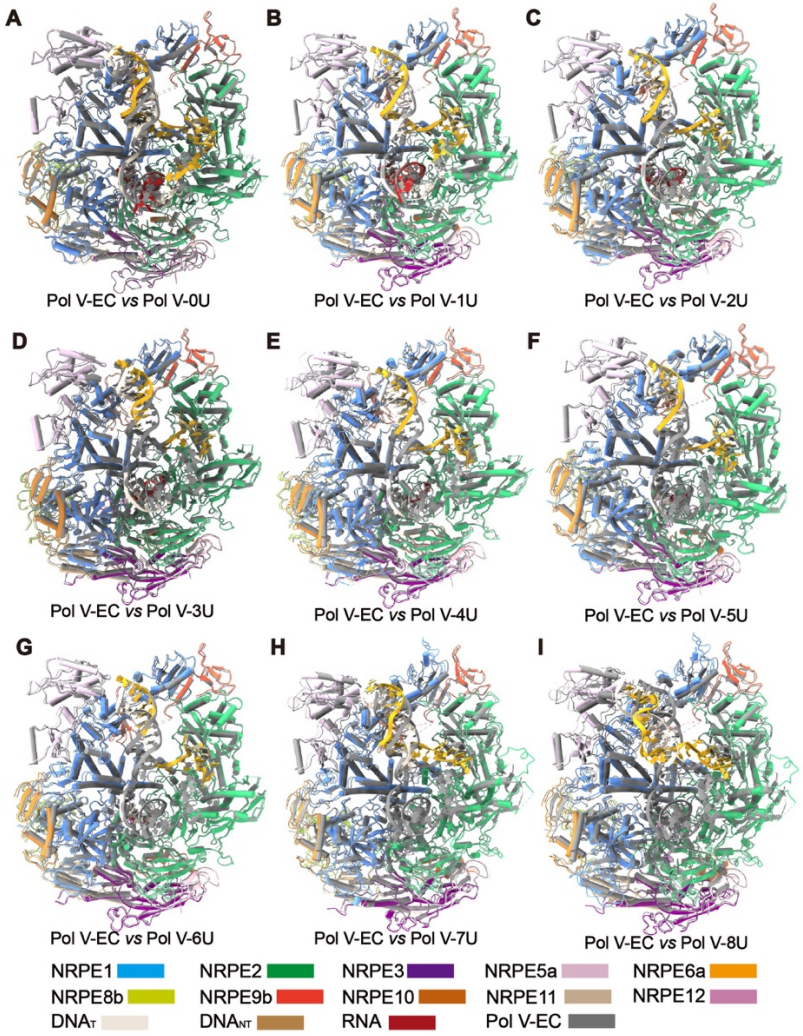


**Appendix Figure S14. The structures of 0U to 8U complexes and their comparison with the Pol V elongation conformation.**

**(A-I)** The superimpositions of 0U (A), 1U (B), 2U (C), 3U (D), 4U (E), 5U (F), 6U (G), 7U (H), and 8U (I) complex structures (in color) to the reported Pol V elongation conformation structure (Pol V-EC, in silver, PDB code: 8HIM) revealed almost identical conformations of Pol V during the termination.

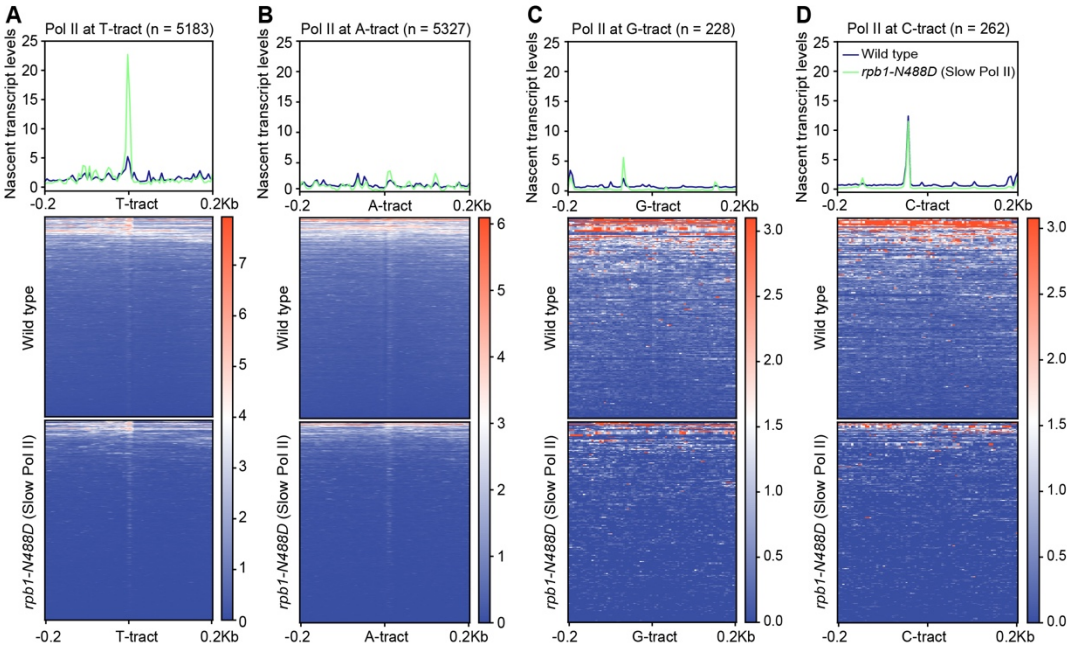


**Appendix Figure S15. Slow RNA Pol II of yeast (*S. pombe*) pauses at the T-tract.** **(A-D)** Metaplot showing the signal of wild-type RNA Pol II (blue) and slow Pol II (*rpb1-N488D*, green) NET-seq at non-template strand T-tract (>5 mer) (A), A-tract (>5 mer) (B), G-tract (>5 mer) (C) and C-tract (>5 mer) (D) at gene 3'-end. Poly(T/A/G/C) tracts are identified within 1Kb around the putative polyadenylation site, and the position of the maximum number of repeats was marked as the center for the metaplot.

**Appendix Table S1. Oligos used in this research**

| Name | Sequence | Use |
|---|---|---|
| **DNA** | | |
| SF-0U-T | AAGCAAAAAAAAAACGGCCTGGTCATTACGAGTA | EM |
| SF-0U-NT | TACTCGTAAGCTAGTATTGATTTTTTTTTTGCTT | EM |
| SF-1U-T | AAGCTCAAGTACTTAAAGCGTCGCATTACGAGTA | EM |
| SF-1U-NT | TACTCGTAAGTGCCTAGCACAAGTACTTGAGCTT | EM |
| SF-2U-T | AAGCTCAAGTACTTAAAACGTCGCATTACGAGTA | EM |
| SF-2U-NT | TACTCGTAAGTGCCTAGCACAAGTACTTGAGCTT | EM |
| SF-3U-T | AAGCTCAAGTACTTAAAAAGTCGCATTACGAGTA | EM |
| SF-3U-NT | TACTCGTAAGTGCCTAGCACAAGTACTTGAGCTT | EM |
| SF-4U-T | AAGCTCAAGTACTTAAAAAATCGCATTACGAGTA | EM |
| SF-4U-NT | TACTCGTAAGTGCCTAGCACAAGTACTTGAGCTT | EM |
| SF-5U-T | AAGCTCAAGTACTTAAAAAAACGCATTACGAGTA | EM |
| SF-5U-NT | TACTCGTAAGTGCCTAGCACAAGTACTTGAGCTT | EM |
| SF-6U-T | AAGCTCAAGTACTTAAAAAAAAGCATTACGAGTA | EM |
| SF-6U-NT | TACTCGTAAGTGCCTAGCACAAGTACTTGAGCTT | EM |
| SF-7U-T | AAGCTCAAGTACTTAAAAAAAAACATTACGAGTA | EM |
| SF-7U-NT | TACTCGTAAGTGCCTAGCACAAGTACTTGAGCTT | EM |
| SF-8U-T | AAGCTCAAGTACTTAAAAAAAAAAATTACGAGTA | EM |
| SF-8U-NT | TACTCGTAAGAGCCTAGCACAAGTACTTGAGCTT | EM |
| SF-1-T | AAGCTCAAGTACTTCGGCCTGGTCATTACGAGTA | Assay |
| SF-1-NT | TACTCGTAAGCTAGTATTGAAAGTACTTGAGCTT | Assay |
| SF-2-T | AAGCTCAAGTACTTAAAAAAAAACATTACGAGTA | Assay |
| SF-2-NT | TACTCGTAAGTGCCTAGCACAAGTACTTGAGCTT | Assay |
| SF-3-T | AAGCTCAAGTACTTCGTCCTGGTCATTACGAGTA | Assay |
| SF-3-NT | TACTCGTAAGTTTTTTTTTTAAGTACTTGAGCTT | Assay |
| SF-4-T | AAGCTCAAGTACTTCGACCAGGACATTACGAGTA | Assay |
| SF-4-NT | TACTCGTAAGAAAAAAAAAAAAGTACTTGAGCTT | Assay |
| SF-5-T | AAGCAAAAAAAAAACGGCCTGGTCATTACGAGTA | Assay |
| SF-5-NT | TACTCGTAAGCTAGTATTGATTTTTTTTTTGCTT | Assay |
| SF-6-T | AAGCTTTTTTTTTTCGGCCTGGTCATTACGAGTA | Assay |
| SF-6-NT | TACTCGTAAGCTAGTATTGAAAAAAAAAAAGCTT | Assay |
| SF-7-T | AAGCTCAAGTACTTTTTTTTTTTCATTACGAGTA | Assay |
| SF-7-NT | TACTCGTAAGTGCCTAGCACAAGTACTTGAGCTT | Assay |
| SF-8-T | AAGCTCAAGTACTTTATATATATAATTACGAGTA | Assay |
| SF-8-NT | TACTCGTAAGTGCCTAGCACAAGTACTTGAGCTT | Assay |
| SF-9-T | AAGCTCAAGTACTTTATTTTAAAAATTACGAGTA | Assay |
| SF-9-NT | TACTCGTAAGTGCCTAGCACAAGTACTTGAGCTT | Assay |
| **RNA** | | |
| RNA-0U | UAUAUGCAGAAAGACCAGGC | EM |
| RNA-1U | UAUAUGCAGAAAGCGACGCU | EM |
| RNA-2U | UAUAUGCAGAAAGCGACGUU | EM |

| | | |
|---|---|---|
| RNA-3U | UAUAUGCAGAAAGCGACUUU | EM |
| RNA-4U | UAUAUGCAGAAAGCGAUUUU | EM |
| RNA-5U | UAUAUGCAGAAAGCGUUUUU | EM |
| RNA-6U | UAUAUGCAGAAAGCUUUUUU | EM |
| RNA-7U | UAUAUGCAGAAAGUUUUUUU | EM |
| RNA-8U | UAUAUGCAGAAAUUUUUUUU | EM |
| RNA-20nt | FAM-UAUAUGCAUAAAGACCAGGC | Assay |
| RNA-SF-1 | FAM-UAUAUGCAGAAAGACCAGGC | Assay |
| RNA-SF-2 | FAM-UAUAUGCAGAAAGUUUUUUU | Assay |
| RNA-SF-3 | FAM-UAUAUGCAGAAAGACCAGGA | Assay |
| RNA-SF-4 | FAM-UAUAUGCAGAAAGUCCUGGU | Assay |
| RNA-SF-5 | FAM-UAUAUGCAGAAAGACCAGGC | Assay |
| RNA-SF-6 | FAM-UAUAUGCAGAAAGACCAGGC | Assay |
| RNA-SF-7 | FAM-UAUAUGCAGAAAGAAAAAAA | Assay |
| RNA-SF-8 | FAM-UAUAUGCAGAAAUAUAUAUA | Assay |
| RNA-SF-9 | FAM-UAUAUGCAGAAAUUUUAAAA | Assay |

**Appendix Table S2. Cryo-EM data collection, refinement, and validation statistics.**

| | 0U complex | 1U complex | 2U complex | 3U complex | 4U complex | 5U complex | 6U complex | 7U complex | 8U complex |
|---|---|---|---|---|---|---|---|---|---|
| EMDB code | EMD-61961 | EMD-61962 | EMD-61963 | EMD-61964 | EMD-61965 | EMD-61966 | EMD-61967 | EMD-61968 | EMD-61969 |
| PDB code | 9K11 | 9K12 | 9K13 | 9K14 | 9K15 | 9K16 | 9K17 | 9K18 | 9K19 |
| **Data collection and processing** | | | | | | | | | |
| Microscopy | Titan Krios (SUSTech #2) | Titan Krios (PKU-IAAS) | Titan Krios (PKU-IAAS) | Titan Krios (PKU-IAAS) | Titan Krios (PKU-IAAS) | Titan Krios (PKU-IAAS) | Titan Krios (PKU-IAAS) | Titan Krios (SUSTech #2) | Titan Krios (SUSTech #2) |
| Voltage (kV) | 300 | 300 | 300 | 300 | 300 | 300 | 300 | 300 | 300 |
| Camera | Gatan K3 | Gatan K3 | Gatan K3 | Gatan K3 | Gatan K3 | Gatan K3 | Gatan K3 | Gatan K3 | Gatan K3 |
| Magnification | 81,000 | 81,000 | 81,000 | 81,000 | 81,000 | 81,000 | 81,000 | 81,000 | 81,000 |
| Pixel size (Å/pixel) | 1.095 | 1.095 | 1.095 | 1.095 | 1.095 | 1.095 | 1.095 | 1.095 | 1.095 |
| Electron exposure ($e^-/Å^2$) | 50 | 50 | 50 | 50 | 50 | 50 | 50 | 50 | 50 |
| Exposure rate ($e^-/A^2/sec$) | 20 | 20 | 20 | 20 | 20 | 20 | 20 | 20 | 20 |
| Frames per movie (no.) | 32 | 32 | 32 | 32 | 32 | 32 | 32 | 32 | 32 |
| Defocus range (μm) | -1.0 to -2.5 | -1.0 to -2.5 | -1.0 to -2.5 | -1.0 to -2.5 | -1.0 to -2.5 | -1.0 to -2.5 | -1.0 to -2.5 | -1.0 to -2.5 | -1.0 to -2.5 |
| Automation software | EPU | EPU | EPU | EPU | EPU | EPU | EPU | EPU | EPU |
| Energy filter slit width (eV) | 20 | 20 | 20 | 20 | 20 | 20 | 20 | 20 | 20 |
| Micrographs (no.) | 2,808 | 4,912 | 3,269 | 7,645<br>3,995 | 3,423 | 3,282 | 6,505 | 2,566 | 9,485<br>6,132 |
| Micrographs used (no.) | 2,808 | 4,912 | 3,269 | 11,640 | 3,423 | 3,282 | 6,505 | 2,566 | 15,617 |
| Total Extracted particles (no.) | 2,466,648 | 3,178,690 | 1,173,619 | 4,736,454<br>1,804,524 | 2,295,354 | 2,090,797 | 4,384,084 | 2,362,323 | 5,533,626<br>5,846,258 |
| **For each reconstruction** | | | | | | | | | |
| Refined particles (no.) | 77,772 | 79,987 | 46,670 | 28,375 | 39,800 | 59,869 | 70,717 | 62,139 | 27,211 |
| Final particles (no.) | 77,772 | 79,987 | 46,670 | 28,375 | 39,800 | 59,869 | 70,717 | 62,139 | 27,211 |
| Data processing software | Relion3.1 | Relion3.1 | Relion3.1 | Relion3.1 | Relion3.1 | Relion3.1 | Relion3.1 | Relion3.1 | Relion3.1 |

| | | | | | | | | | |
|---|---|---|---|---|---|---|---|---|---|
| Point group | *C*1 | *C*1 | *C*1 | *C*1 | *C*1 | *C*1 | *C*1 | *C*1 | *C*1 |
| Resolution (global, Å) | 2.96 | 3.46 | 3.04 | 3.73 | 3.32 | 3.19 | 3.04 | 3.42 | 4.06 |
| FSC 0.143 (unmasked/masked) | 3.8/2.96 | 4.13/3.46 | 4.03/3.04 | 4.59/3.73 | 4.17/3.32 | 3.96/3.19 | 3.84/3.04 | 4.21/3.42 | 7.46/4.06 |
| FSC 0.5 (unmasked/masked) | 7.3/3.43 | 8.22/4.11 | 8.2/3.61 | 9.9/4.5 | 8.4/3.98 | 7.81/3.79 | 7.14/3.57 | 8.06/3.91 | 11.36/7.46 |
| Local resolution range (Å) | 2.8-5.0 | 3.0-5.0 | 3.0-7.0 | 3.5-7.0 | 3.0-7.0 | 3.0-5.0 | 3.0-5.0 | 3.4-5.5 | 4.0-8.0 |
| Map sharpening B-factor ($Å^2$) | -35 | -60 | -30 | -60 | -57 | -30 | -40 | -56 | -60 |
| Map sharpening methods | Half-maps correlation | Half-maps correlation | Half-maps correlation | Half-maps correlation | Half-maps correlation | Half-maps correlation | Half-maps correlation | Half-maps correlation | Half-maps correlation |
| **Refinement** | | | | | | | | | |
| Refinement package | Phenix | Phenix | Phenix | Phenix | Phenix | Phenix | Phenix | Phenix | Phenix |
| - real or reciprocal space | Real space | Real space | Real space | Real space | Real space | Real space | Real space | Real space | Real space |
| - resolution cutoff (Å) | 3.0 | 3.5 | 3.04 | 3.8 | 3.3 | 3.19 | 3.04 | 3.5 | 4.1 |
| Model-Map scores | | | | | | | | | |
| - CC | 0.85 | 0.62 | 0.77 | 0.61 | 0.78 | 0.81 | 0.82 | 0.80 | 0.58 |
| No. atoms | | | | | | | | | |
| Protein / nucleotides | 22,609/1,307 | 22,512/1307 | 22,575/908 | 22,431/768 | 22,612/485 | 22,564/615 | 22,568/574 | 23,005/696 | 22,734/653 |
| $Mg^{2+}$ / $Zn^{2+}$ | 1/6 | 1/6 | 1/6 | 1/6 | 1/6 | 1/6 | 1/6 | 1/6 | 1/6 |
| *B*-factors ($Å^2$) | | | | | | | | | |
| Protein / nucleotides | 88.7/124.4 | 134.4/113.0 | 81.6/67.4 | 111.0/92.6 | 77.0/121.4 | 105.8/124.1 | 101.9/105.2 | 88.4/77.3 | 121.4/125.2 |
| $Mg^{2+}$ / $Zn^{2+}$ | 141.1 | 189.9 | 167.0 | 184.7 | 161.0 | 200.3 | 224.5 | 117.6 | 137.7 |
| R.m.s. deviations | | | | | | | | | |
| Bond lengths (Å) | 0.003 | 0.003 | 0.003 | 0.005 | 0.004 | 0.003 | 0.003 | 0.004 | 0.005 |
| Bond angles (°) | 0.621 | 0.684 | 0.647 | 0.817 | 0.599 | 0.664 | 0.647 | 0.677 | 0.889 |

| **Validation** | | | | | | | | | |
|---|---|---|---|---|---|---|---|---|---|
| MolProbity score | 1.65 | 1.73 | 1.67 | 2.17 | 1.99 | 1.59 | 1.57 | 2.10 | 2.24 |
| Clashscore | 5.40 | 7.88 | 5.39 | 12.96 | 6.17 | 6.08 | 5.47 | 6.44 | 13.83 |
| Poor rotamers (%) | 0.80 | 0.84 | 1.23 | 1.40 | 2.36 | 0.84 | 1.12 | 1.79 | 0.00 |
| C-beta outlier (%) | 0.00 | 0.00 | 0.00 | 0.00 | 0.00 | 0.00 | 0.00 | 0.00 | 0.00 |
| CaBLAM outliers | 2.93 | 2.54 | 2.54 | 3.19 | 2.42 | 2.94 | 2.61 | 5.62 | 6.47 |
| Ramachandran plot | | | | | | | | | |
| Favored (%) | 94.8 | 95.7 | 95.6 | 93.4 | 94.6 | 96.2 | 96.4 | 89.8 | 88.2 |
| Allowed (%) | 5.2 | 4.3 | 4.4 | 6.6 | 5.4 | 3.8 | 3.6 | 10.2 | 11.7 |
| Outlier (%) | 0.0 | 0.0 | 0.0 | 0.0 | 0.0 | 0.0 | 0.0 | 0.0 | 0.1 |